ADVANCED OPTICAL MATERIALS
www.advopticalmat.de

Underwater Self-Powered All-Optical Wireless Ultrasonic Sensing, Positioning and Communication with Ultrafast Response Time and Ultrahigh Sensitivity

Zhen Tian, Li Su, Haoyu Wang, Hongqiang Wang, and Yunlong Zi**

The utilization of ultrasonic waves in the ocean has become an attractive topic for its applications in underwater sensor networks via a variety of research methods, such as sensing, positioning, and communication. However, it is still challenging to develop a cost-effective, stable, fast, and accurate wireless underwater ultrasonic device with self-power-ability in various circumstances. Herein, a novel underwater self-powered all-optical wireless ultrasonic sensor (SAWS) based on triboelectrification-induced electroluminescence (TIEL) has been proposed, in which efficient and stable TIEL can be generated under the excitation of ultrasonic waves. The SAWS has been demonstrated to accurately determine the location of the ultrasonic source with an error of less than 4.6%, and as a promising candidate for real-time optical signal communication with an ultrafast response time of below 50 ms and an ultrahigh signal-to-noise ratio (SNR) of 26.02 dB. To date, the paradigm-shift strategy for underwater ultrasonic sensing has been developed for the first time to be fully self-powered without any wire connections. The SAWS proposed here paves a new path to the realization of a self-powered underwater all-optical wireless sensing system that can be effectively applied in underwater environmental monitoring, underwater robots, ocean sensor networks, etc.

1. Introduction

The rapid development of ocean exploration by human beings is accompanied by the high demand for underwater ultrasonic technology which has the advantages of high transmission efficiency and biological safety, strong penetration, no electromagnetic interference (EMI) as well as long transmission distance.[1–5] The significant progress of ultrasonic technology has been widely used in applications such as energy harvesting[6] and transmission,[7] target detection,[8] and signal communication,[9] thus turning into a hot research topic in recent years. Until now, most existing ultrasonic sensors rely on the piezoelectric effect created by certain materials such as barium titanate ($BaTiO_3$) ferroelectric ceramics,[10–12] lead zirconate titanate (PZT) piezoelectric ceramics,[13–15] or other bulk materials.[16,17] Recently, triboelectric nanogenerators (TENGs) have been developed as an effective alternative solution to convert mechanical energy into electricity so as to generate the voltage of a few hundred volts in just milliseconds, with a wide-range options of materials offered.[18–20] On the basis of this emerging technology, different strategies have been devised to promote the outcome of ultrasonic energy harvesting and sensing through a wide variety of TENG designs.[21–24] Nevertheless, these ultrasonic devices commonly rely on the wired communication of electrical signals, which is constrained by the limited communication distance and impact of EMI, and the application scope is also restricted by complex manufacturing process, high expense, and huge maintenance cost. Therefore, it is urgent to develop a long-distance, EMI-free, fast, and self-powered underwater ultrasonic sensing & communication device without any external wire connections through a paradigm-shift strategy.

Triboelectrification-induced electroluminescence (TIEL) is an emerging concept of luminescence initiated by extremely gentle mechanical interactions,[25,26] where the surface charges generated by the triboelectric effect can abruptly and greatly change the surrounding electric field, which thus excites the electroluminescence (EL) of underlying phosphors. Nowadays, it has attracted widespread attention due to its superiority in

Z. Tian, L. Su
College of Physics Science and Technology
Institute of Life Science and Green Development
Hebei University
Baoding, Hebei 071002, China
E-mail: suli@hbu.edu.cn

H. Wang
Shenzhen Key Laboratory of Biomimetic Robotics and Intelligent Systems
Department of Mechanical and Energy Engineering
Southern University of Science and Technology
Shenzhen, Guangdong 518055, China

L. Su, H. Wang, Y. Zi
Department of Mechanical and Automation Engineering
The Chinese University of Hong Kong
New Territories, Shatin, Hong Kong, China
E-mail: ylzi@cuhk.edu.hk

The ORCID identification number(s) for the author(s) of this article can be found under https://doi.org/10.1002/adom.202102091.

DOI: 10.1002/adom.202102091

many aspects, including low threshold, high responsiveness, and non-destructive operation as compared to traditional mechanoluminescence (ML).[27,28] It has been reported to be excited by wind,[29] water[30] and human motion,[31] with its applications demonstrated in stress sensors,[32] display,[33] illumination[34] and human-machine interface.[35,36] Based on these characteristics, TIEL is expected to respond to underwater ultrasonic waves in order to realize optical wireless communication, which is advantaged by ultrahigh transmission speed, ultrafast response time, ultrahigh sensitivity, wide radiation range, environmentally friendly and safety, etc.

In this work, an underwater self-powered all-optical wireless ultrasonic sensor (SAWS) based on TIEL was developed with the capability of generating efficient and stable TIEL in response to underwater ultrasonic waves. Here, the performance of the TIEL material was optimized by introducing electrospun nanofibers and a cavity structure between its interfaces. Among them, EL particles in the cylindrical cavity were periodically contacted and separated between top and bottom triboelectrification layers under ultrasonic wave excitation, and then the alternating electric field was generated to excite EL. Three SAWSs were used to construct a multichannel ultrasonic sensor system to position the ultrasonic source within an error of less than 4.6%. Via a self-developed software interface, real-time underwater optical signal communication was achieved with an ultrafast response time of below 50 ms and an ultrahigh signal-to-noise ratio (SNR) of 26.02 dB, which are advanced compared to previous studies (Table S1, Supporting Information). To conclude, the SAWS has outstanding potential in underwater applications such as ocean environmental monitoring, underwater robotics, and ocean sensor networks, featuring ultra-fast response, ultra-high sensitivity, excellent stability, and high mechanical robustness. While receiving ultrasonic wave excitation from surface ships, underwater vehicles, or marine organisms, the SAWS can transmit the perceived data to intelligent gateway nodes through optical signals to be connected to the ground network and meet practical application requirements, as shown in **Figure 1**a.

2. Results and Discussion

The SAWS consists of a multilayered composite structure, where the layer of electrospun polyvinylidene fluoride (PVDF) nanofibers was assembled between a flexible substrate (fluorinated ethylene propylene (FEP) in this case) and a polyethylene terephthalate (PET) layer drilled with an array of cylindrical holes to form the cavity structure, as shown in Figure 1b. ZnS:Cu phosphors were uniformly filled in the cylindrical cavity as vibration units and a top FEP film was fixed in parallel on the PET layer to isolate and seal the device to be waterproof, working as one of the negative tribo-materials (I: top and II: side views of one SAWS unit in Figure 1b). Here, PVDF nanofibers have excellent mechanical properties, high dielectric strength, and large specific surface area, which can increase the electric field and achieve high-sensitivity TIEL.[37] Under the excitation of underwater ultrasonic waves, ZnS:Cu particles in the cavity acted as positive tribo-materials and could move up and down, eventually colliding with negative tribo-materials PVDF nanofibers and the FEP layer to generate TIEL. Figure 1c and d show the scanning electron microscope (SEM) images of ZnS:Cu particles and PVDF nanofibers with an average diameter of about 40 μm and 250 nm, respectively. Figure 1e confirms that ZnS:Cu particles were distributed on the surface of PVDF nanofibers in the SAWS with cross-sectional SEM image exhibited in Figure 1f, where the sequential distribution of the ultra-thin layered structure (400 μm) can be distinguished. Here d presents the depth (150 μm) of the cylindrical cavity. As demonstrated in Figure 1g, the fabrication process diagram of the SAWS is mainly based on electrospun and hot-pressing technology with the advantages of low cost, practicability, and huge potential in large-scale applications, as the detailed fabrication process is displayed in Experimental Section. The optical transmission spectra of the FEP film and PVDF nanofibers as a luminescence-based sensor are illustrated in Figure 1h. The produced TIEL was emitted outward completely due to the high optical transmittance (95.4% at 510 nm) of the top FEP layer, while PVDF nanofibers worked as the bottom layer because of the inferior transmittance (37.2%). With regard to the design, a photo of the SAWS held on a hand is shown in Figure 1i, suggesting its satisfactory bendability. The X-ray diffraction (XRD) patterns of ZnS:Cu phosphors and PVDF nanofibers are presented in Figure 1j,k, respectively. Three main peaks at 2θ values of 28.8°, 48.3° and 56.09° corresponded to the (111), (220) and (311) lattice planes of the zinc-blended structure of ZnS. The 2θ value at 20.26° corresponds to the (110) lattice planes of the β-phase PVDF.[38] In order to determine the impact of the piezoelectric property of the β-phase PVDF (piezoelectric phase) on the luminescence intensity of the SAWS, two control devices with the above-mentioned PVDF and polyvinyl chloride (PVC) nanofibers without piezoelectric property were prepared, showing obvious EL effect, as exhibited in Figure S1 (Supporting Information). The result indicates that the luminescence intensity of the SAWS mainly derived from the triboelectric effect while the piezoelectric effect was not necessary. Figure 1l,m presents the photographs of a luminescent array (4 × 4) and a letter "D" under underwater ultrasonic wave excitation (refer to Movie S1 and S2, Supporting Information), indicating that the SAWS array can be tailored into different patterns according to actual needs. Significantly, other forms of vibration such as wind energy can also drive the SAWS, as shown in Movie S3 (Supporting Information).

To reveal the working mechanism of the SAWS, four different devices marked with I (without nanofibers or cavity structure), II (only with PVDF nanofibers), III (only with cavity structure), and IV (with PVDF nanofibers and cavity structure) were prepared for comparison, as presented in **Figure 2**a. The corresponding emission spectra of the given devices are shown in Figure 2b, and the construction of the test platform is exhibited in Figure S2 (Supporting Information). As for device I, negligible luminescence was observed from the incomplete contact-separation between ZnS:Cu particles and two triboelectrification layers. Regarding device II, luminescence was slightly enhanced by a larger contact area provided by PVDF nanofibers. Concerning device III, a more observable TIEL was produced due to more sufficient vibration space created by the cylindrical cavity structure. Device IV showed the highest intensity, indicating that PVDF nanofibers and cavity structure

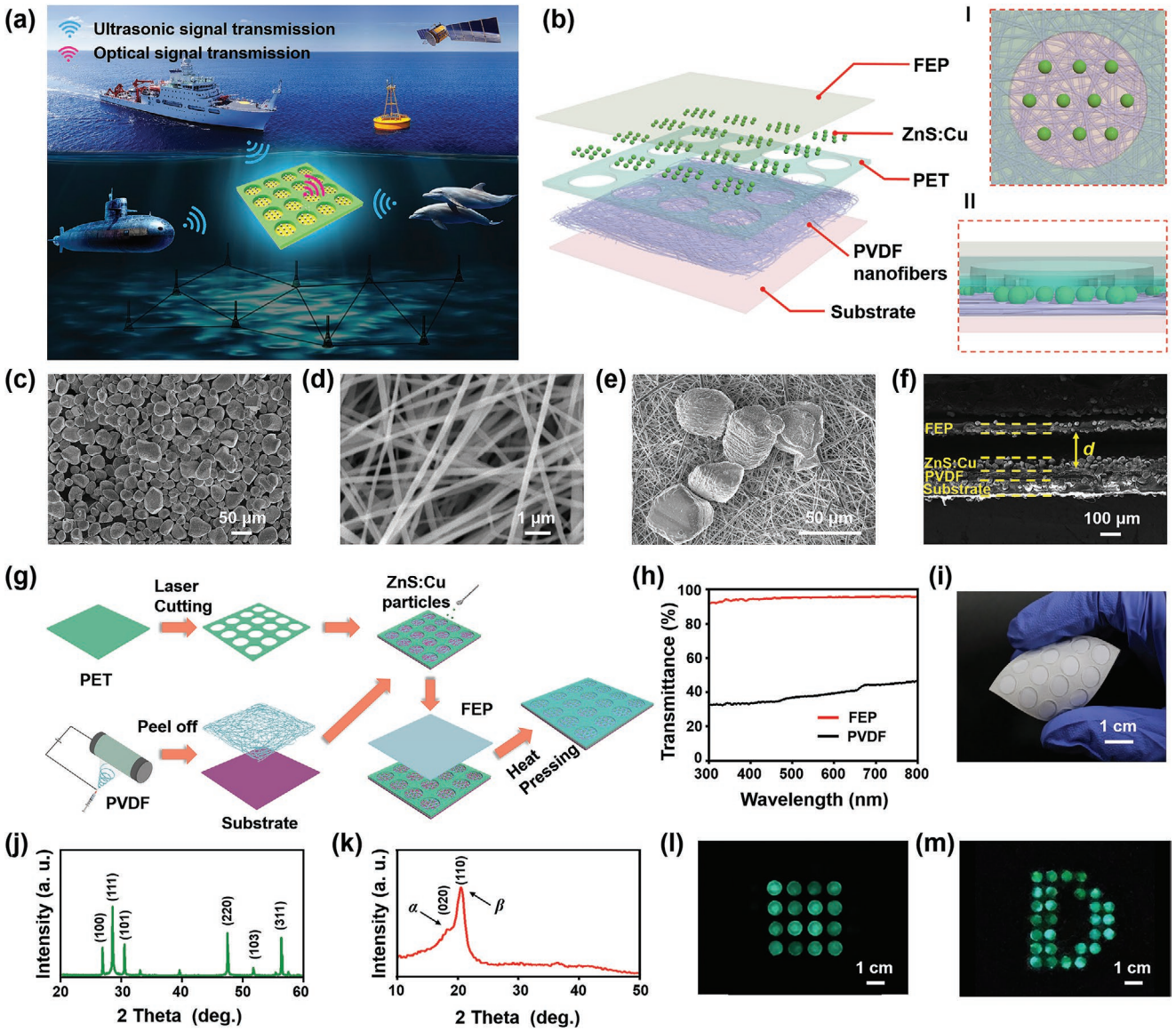

Figure 1. Conceptual and structural design of the SAWS. a) Conceptual diagram of the SAWS capable of converting ultrasonic waves energy into visible light signals for sensing, positioning, and communication. b) Structure diagram of the SAWS constructed layer by layer (I: top and II: side views of one cavity unit). SEM image of c) ZnS:Cu phosphors, d) PVDF nanofibers, and e) ZnS:Cu particles distributed on PVDF nanofibers. f) Cross-sectional SEM image of the SAWS (*d* refers to the depth of the cavity). g) Fabrication process diagram of the SAWS. h) Transmittance spectra of the FEP film and PVDF nanofiber membrane. i) Photograph of a bent device held in a hand. XRD patterns of j) ZnS:Cu phosphors and k) PVDF nanofibers. Luminous photographs of l) the 4 × 4 array and m) the letter "D" under underwater ultrasonic wave excitation.

were both conducive to significantly promoting tribo-charges, thereby exciting EL phosphors. Based on the aforementioned results, the whole luminescence generation process of the SAWS is illustrated in Figure 2c, which includes four typical states in a complete working cycle. Under ultrasonic wave excitation, ZnS:Cu particles constantly moved up and down, colliding the FEP film and PVDF nanofibers. Due to the extremely strong electronegativity of the FEP film and PVDF nanofibers, electrons were injected from ZnS:Cu phosphors into the FEP film and PVDF nanofibers while coming into contact with them. The surface of ZnS:Cu phosphors accumulated equal amounts of positive charges. In this process, the electric field on ZnS:Cu phosphors can be dynamically changed, which reaches the minimum value when in contact with the bottom nanofibers (states I) and rapidly raises to the maximum when in contact with the top triboelectrification layer (states III). Consequently, the EL of ZnS:Cu phosphors was excited by the dynamic electric field. The distribution of the electric field and potential on ZnS:Cu phosphors within a full contact-separation cycle was verified by establishing a two-dimensional (2D) model of SAWS in cross-section through finite element simulation using COMSOL software, as shown in Figure 2d and Figure S3 (Supporting Information). The simulation results indicate that the variation of the electric field (ΔE) and potential (ΔV) of ZnS:Cu phosphors along the dashed lines reached 2.3 MV m^{-1} and 452 V in one working cycle, respectively, thus providing a

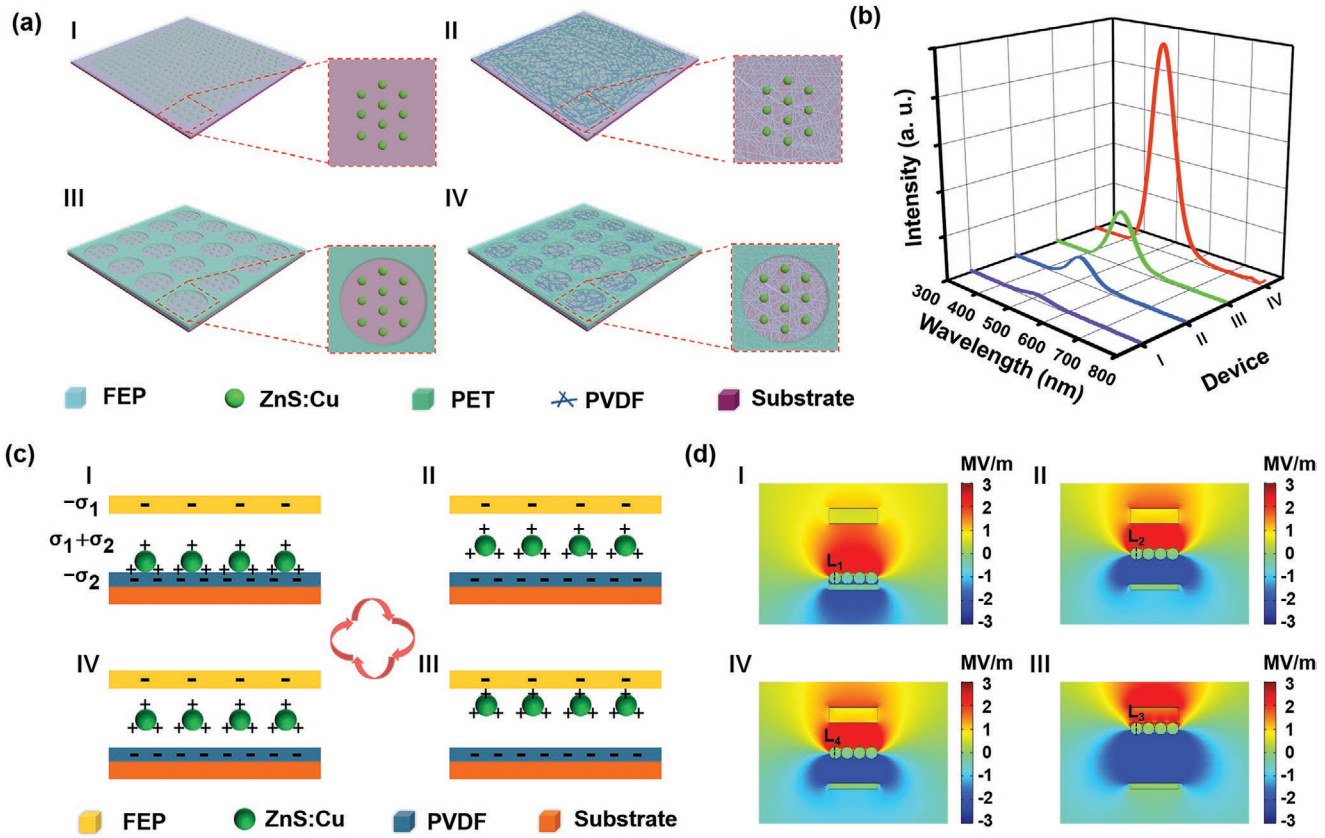

Figure 2. Working mechanism of the SAWS. a) Four control devices used to identify potential working mechanisms (I: without nanofibers or cavity structure; II: only with PVDF nanofibers; III: only with cavity structure; IV: with PVDF nanofibers and cavity structure simultaneously). b) Corresponding emission spectra of four control devices. c) Schematic diagram of the working mechanism of the SAWS. d) Numerical calculation of the electric field distribution of ZnS:Cu phosphors in four states within a full contact-separation working cycle using COMSOL software.

powerful support for the proposed working mechanism of TIEL in Figure 2c.

The EL principle of ZnS:Cu phosphors is shown in the band diagram in **Figure 3**a. Owing to the excitation of the alternating electric field, electrons were animated into shallow electron trap states (blue) and then fell into the Cu energy level (red), resulting in green luminescence. According to Figure 3b, the wavelength peak of the TIEL of the SAWS was centered at 510 nm under ultrasonic waves excitation, corresponding to the chromaticity diagram color coordinates of (0.20, 0.47) with a blue-green light (inset of Figure 3b). Besides, it was also demonstrated that ZnS:Cu phosphors can be excited by applying external stimuli such as photons, electric field and stress, which are known as photoluminescence (PL), EL, and ML, respectively, and whose corresponding emission spectra are shown in Figure 3c, where the detailed experimental explanation is illustrated in Note S1 (Supporting Information). The wavelength peaks of EL, PL, and ML were all approximately concentrated at 520 nm. These results were compared with TIEL, indicating that the slight wavelength difference (about 10 nm) was attributed to the different probabilities of the electron transition from the shallow electron trap to the t_2 or e state of Cu^{2+}, driven by the high-frequency ultrasonic waves.[39]

Moreover, several groups of control experiments were set up in order to investigate the major influential factors for the TIEL intensity of the SAWS. In terms of the cavity structure, first, the emission spectra with different cavity diameters and PET thicknesses were shown in Figure 3d,e. Based on the results, the cavity has an optimal area of 0.5 cm^2 and an optimal thickness of 150 μm to achieve the strongest TIEL intensity. Second, the filling ratio (F) of phosphors in each unit profoundly affected luminescence intensity, which can be calculated by:

$$F = \frac{V_{ZnS}}{V_{cavity}} \tag{1}$$

where V_{ZnS} and V_{cavity} are the volumes of ZnS:Cu powders and the cavity structure, respectively. As shown in Figure 3f, luminescence intensity increased first and then decreased with the gradual increase of F. Here, ZnS:Cu phosphors cannot provide enough surface area for triboelectrification when F is too small, and they cannot vibrate actively when F is too large, which both exhibit weak luminescence intensity, as illustrated in Figure S4 and Note 2 (Supporting Information). As a result, the SAWS has the optimal F of around 50% to maximize luminescence intensity. Third, the impact of the liquid environment on the luminescence intensity of the SAWS was investigated. Five different types of liquids were selected as environment media including deionized (DI) and tap water, pure ethanol (absolute value ≥ 99.5%, Macklin),

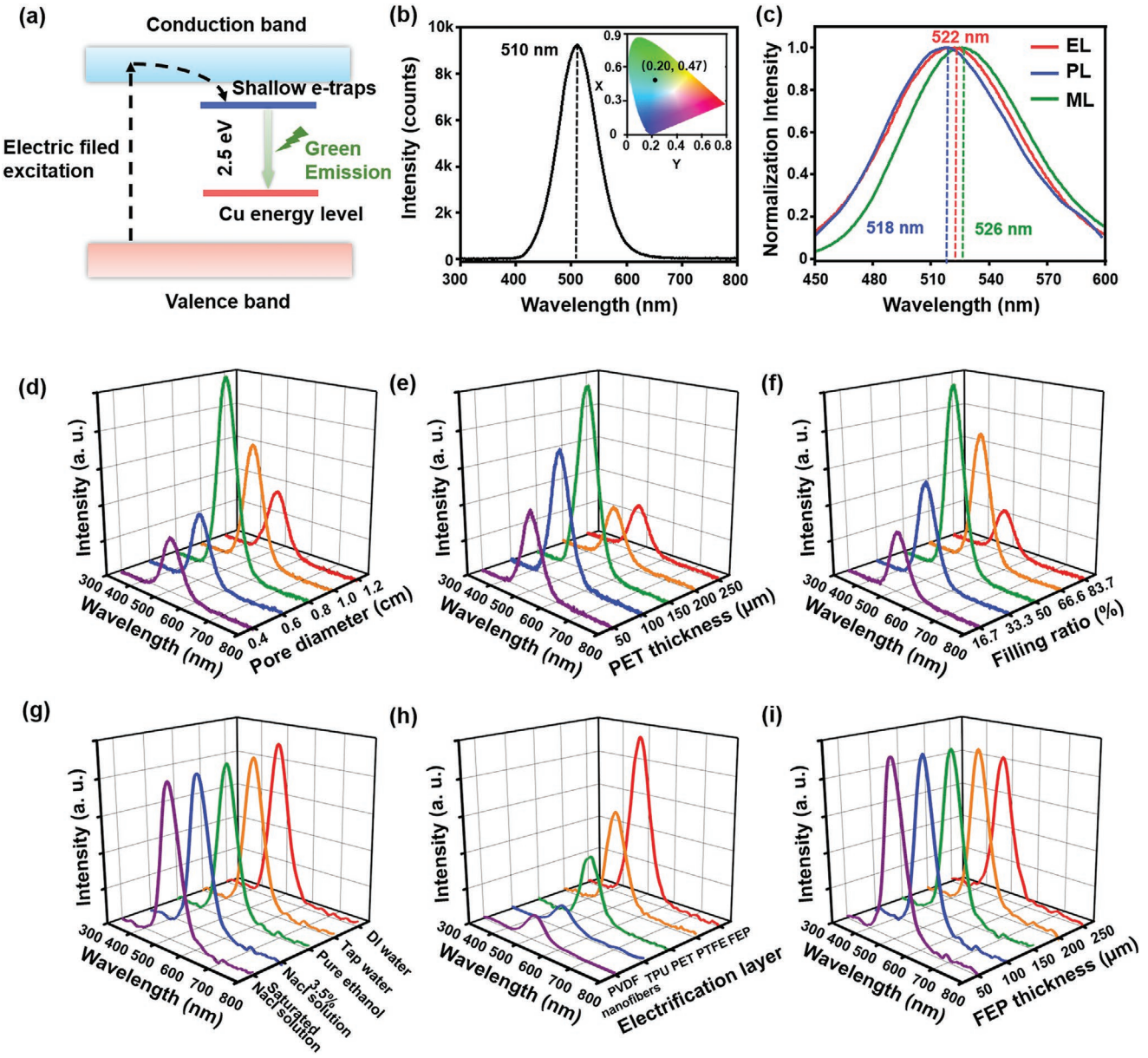

Figure 3. Experiment measurement results of the SAWS. a) Schematic diagram of the EL principle of ZnS:Cu phosphors. b) Emission spectrum of TIEL in this case. Inset: Corresponding color coordinates. c) Emission spectra of EL, PL and ML for ZnS:Cu phosphors. Dependence of TIEL intensity on the d) diameter, e) thickness and f) filling ratio (*F*) of the cavity. Dependence of TIEL intensity on the g) liquid medium, h) top tribo-material, and i) thickness of the FEP film.

3.5% and saturated sodium chloride solutions, and the experimental results are shown in Figure 3g. The luminescence intensities generated by the SAWS in all of the five solutions were basically the same, which suggested that the liquid type has little influence on the operation of the SAWS, indicating that SAWSs can be applied in a variety of liquid environments. Fourthly, the types and thickness of the tribo-material layer were studied due to their impact on the tribo-charges. To investigate the influence of the top tribo-material, five types of materials were selected for measurement, including thermoplastic polyurethanes (TPU), PET, polytetrafluoroethylene (PTFE), FEP, and PVDF nanofibers. As shown in Figure 3h, the intensity of TPU to FEP gradually increased due to the enhancement of contact electrification, which satisfied the "triboelectric series".[40] Although the tribo-charges generated in PVDF nanofibers were stronger than that in the compact FEP film, PVDF nanofibers cannot be used as the top tribo-material on account of their poor transmittance (Figure 1h). Meanwhile, the influence of the thickness of the top tribo-material layer was investigated as well. Figure 3i illustrates the effect of the thickness of the FEP film on the luminescence intensity of the SAWS, where it slightly decreased with the increase of the thickness from 50 to 250 μm, which can be attributed to the small loss of transmittance.

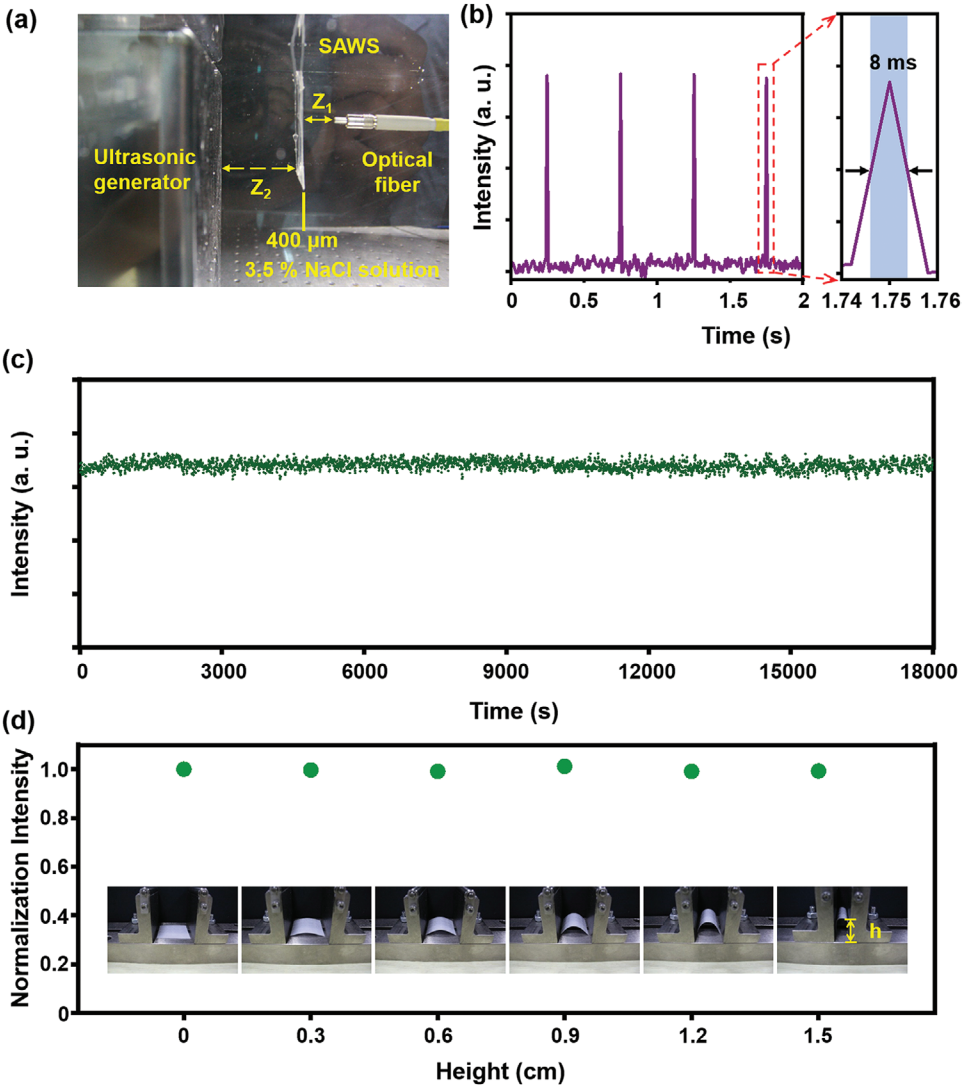

Figure 4. The responsiveness, stability, and flexibility of the SAWS in the natural seawater environment simulated by 3.5% NaCl solution. (a) Side view of an experimental configuration for characterization ($Z_1 = 1$ cm; $Z_2 = 5$ cm). (b) Response time of the SAWS through consecutive emission measurements. (c) Stability of the SAWS during the ultrasonic generator worked continuously for 5 hours. (d) Flexibility of the SAWS.

It is necessary to carefully investigate the responsiveness, stability, and flexibility of the SAWS according to the practical applications. The underwater experiment platform in the natural seawater environment was stimulated by 3.5% NaCl solution, as shown in **Figure 4**a. Ultrasonic wave energy can be generated by an ultrasonic generator with a frequency of 40 kHz and an incident power of 0.6 W cm^{-2}. The response time of the SAWS is shown in Figure 4b by rapidly switching the ultrasonic generator. Considering that the spectrometer in this study has a time resolution of 8 ms, the response time of SAWS is much shorter. The result indicates that the optical signal of the SAWS can rapidly respond to ultrasonic waves, which is an extremely beneficial feature in the field of underwater ultrasonic sensing. Moreover, the optical signal was continuously measured with an interval of 1000 ms for 5 h to verify the stability of the SAWS, as shown in Figure 4c, where the SAWS displayed stable luminescence intensity throughout the whole test, demonstrating excellent stability and repeatability. Due to the excellent hydrophobic property and chemical inertness of the FEP, after being immersed in the 3.5% NaCl solution for one week, SAWS shows no obvious degradation in luminescence intensity (Figure S5, Supporting Information). A bending test was performed to study the flexibility and mechanical robustness of the device, as shown in Figure 4d. When the bending height of the sensor (4×4 cm^2) increased from 0 to 1.5 cm, no apparent decrease in intensity or physical damages can be seen after each bending cycle. It should be mentioned that the ultra-thin (400 μm) film structure makes the SAWS very convenient for packaging, integration and fixation. Packaging with transparent rigid materials can greatly improve the underwater working depth of SAWS in practical applications (Figure S6, S7, and Note 3, Supporting Information). By virtue of these advantages, the SAWS can be fully adapted to the complex underwater environment, which is reliable throughout a long period of operation.

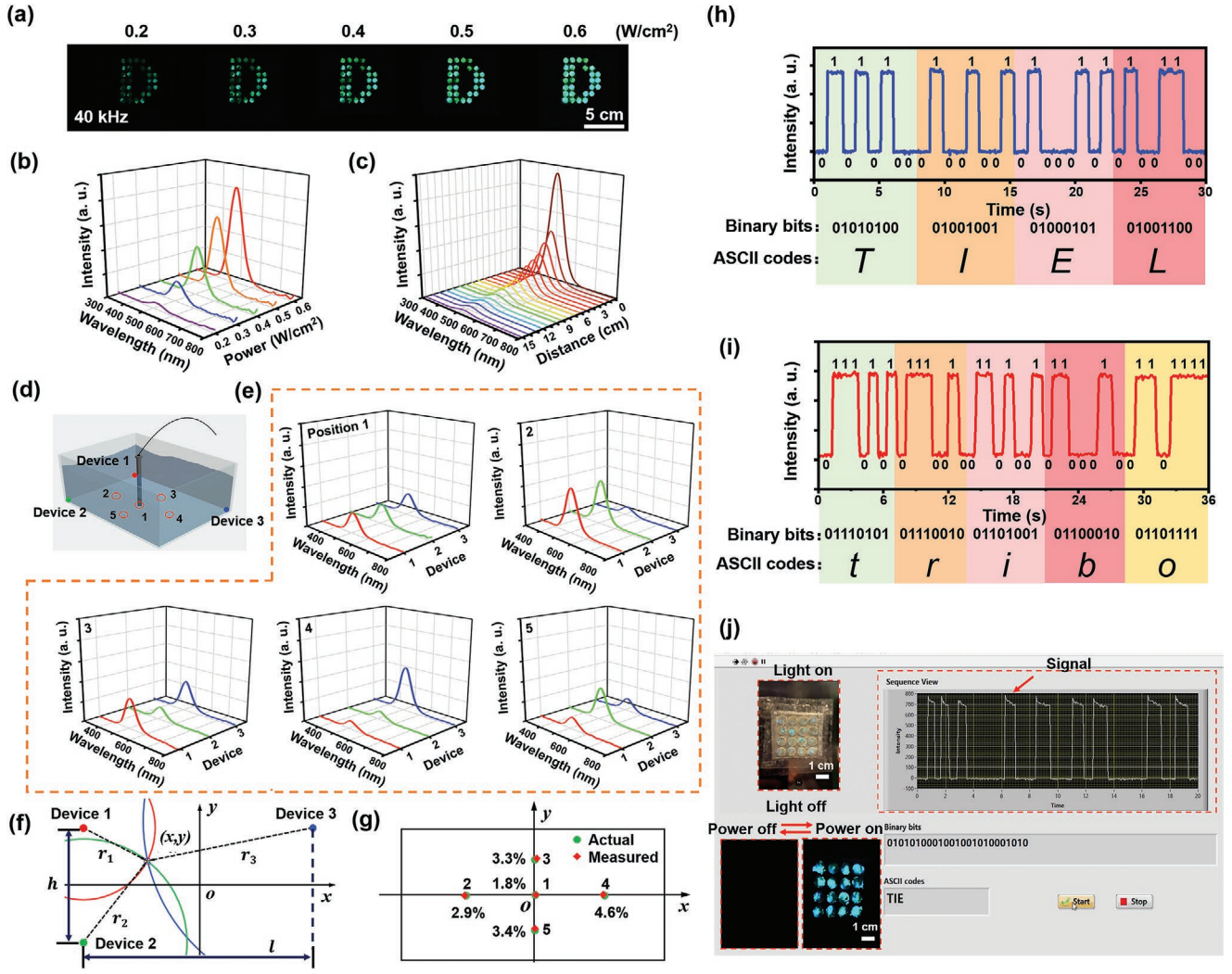

Figure 5. Demonstration of the SAWS in the current study for sensing, positioning, and signal communication. a) Photographs of the SAWS under different ultrasonic powers at 40 kHz. Dependence of luminescence intensity on b) ultrasonic power at 40 kHz and c) the distance from the ultrasonic source at 40 kHz and 0.6 W cm^{-2}. d) Schematic diagram of the positioned experimental setup showing three SAWSs at three different corners in the bottom of a water tank. e) Luminescence intensity at five positions in (d). f) Schematic diagram of the principle based on the three-point location method of determining the ultrasonic source. g) Actual and measured positions of the ultrasonic source and its corresponding positioning error. Continuous optical signals generated by the SAWS and its corresponding retrieval information h) "TIEL" and i) "tribo". j) Real-time data read with a self-developed software interface (programmed by LabVIEW). Inset: Corresponding photographs of the SAWS.

As a proof of concept, the potential applications of the SAWS in underwater (3.5% NaCl solution) self-powered wireless sensing, positioning and signal communication were demonstrated. The luminescent photographs and emission spectra of the SAWS in different ultrasonic power inputs are demonstrated in **Figure 5**a,b, respectively, where the detailed luminescent process is shown in Movie S4 (Supporting Information). It was found that the luminescence intensity of the device linearly increased with the increase of ultrasonic power (40 kHz) at a fixed distance (Figure S8, Supporting Information). Moreover, the luminescence intensity of the SAWS at a varying distance (0 to 15 cm) from the ultrasonic source with an increment of 1 cm was measured (40 kHz, 0.6 W cm^{-2}), as shown in Figure 5c, which is consistent with the equation of ultrasonic attenuation expressed as:

$$I = I_0 e^{-\alpha x} \quad (2)$$

where I_0 and I are the initial intensity ($x = 0$) and intensity at a certain distance (x) from the ultrasonic source; α refers to the attenuation factor of the medium, linearly depending on ultrasonic frequency. By exponentially fitting the data in Figure 5c, α was determined as 0.269 in this case, as shown in Figure S9 (Supporting Information), which verified that the SAWS can be effectively used to detect and locate ultrasonic sources. Here, a multichannel ultrasonic sensor system was built based on the SAWS, as presented in Figure 5d. A cylinder-shaped ultrasonic source (40 kHz, 0.6 W cm^{-2}) was located in the water tank ($30 \times 40 \times 40$ cm^3) to emit ultrasonic waves. Three SAWSs were placed at three corners of the water tank to collect ultrasonic waves, while the generated optical signals were simultaneously

collected by the spectrometer. Five different positions of the ultrasonic source were set at the bottom of the water tank, with details shown by red circles in Figure 5d, where the experimental results for all these positions are shown in Figure 5e. The three-point localization method of determining the ultrasonic source is depicted in Figure 5f, where the difference in the distance from the ultrasonic source to three SAWSs, as the radiuses of the three circles marked as r_1, r_2, and r_3, respectively, can be determined by Equation (2). Then, the ultrasonic source was located at the intersection coordinates (x, y) of the three circles and can be calculated by the equations as follows:

$$\begin{cases} \left(x-\frac{l}{2}\right)^2+\left(y-\frac{h}{2}\right)^2=r_1^2 \\ \left(x+\frac{l}{2}\right)^2+\left(y-\frac{h}{2}\right)^2=r_2^2 \\ \left(x+\frac{l}{2}\right)^2+\left(y+\frac{h}{2}\right)^2=r_3^2 \end{cases} \tag{3}$$

where h is the distance between SAWSs 1 and 2, and l represents the distance between SAWSs 1 and 3. The corresponding experimental results are shown in Figure 5g with location errors of less than 4.6%. Moreover, a customized data acquisition system based on LabVIEW was also applied to visualize and demonstrate the positioning characteristic of SAWS, as presented in Movie S5 (Supporting Information).

The SAWS can be further applied in real-time optical communication, where binary bits "0" and "1" can be identified from the optical signal, as demonstrated by the states "off" and "on" of the TIEL signal of the SAWS. To directly visualize the process of data reading, a computer software interface was programmed by LabVIEW to retrieve the data in real-time with a time interval of 50 ms. The ASCII code was used as the coding strategy here, where eight binary bits (each communication time is 900 ms) stand for a character. For instance, bits "0 101 0100" represent a letter "T". Figure 5h,i shows the continuous spectral signals generated by the SAWS for the code encrypted by the corresponding retrieval information "TIEL" and "tribo", respectively, as illustrated in Figure 5j and Movie S6 (Supporting Information). Upon the completion of data transmission, a character string "TIEL" and the corresponding optical signals were displayed on the software interface with a calculated SNR of 26.02 dB.

3. Conclusions

In this work, SAWS was designed by introducing ZnS:Cu particles into the cavity structure between the top triboelectric layer and bottom nanofibers. Capable of successfully generating effective and stable TIEL under underwater ultrasonic wave excitation, the designed SAWS represents a completely novel sensing paradigm. This research fully studied the working principle of the SAWS and the influential factors of its sensing performance. With the advantages of full-self-power-ability, ultrafast response time, low cost, ultrahigh sensibility, easy manufacturing, environmentally friendly and safety, as well as excellent stability, underwater sensing, positioning and optical communication were demonstrated as proofs of concepts. To sum up, the designed SAWS is a new approach to construct an underwater self-powered all-optical wireless ultrasonic sensing system, which greatly broadens the underwater applications of intelligent optical materials, with significant potential in underwater sensing systems, ocean sensing networks, and ocean robotics.

4. Experimental Section

Preparation of PVDF Nanofibers: PVDF powders (MW ≈ 400000, Macklin) which have a mass fraction of 10% were dissolved into 10 ml of solvent mixture made up of 60% acetone (Kermel) and 40% dimethylformamide (DMF, Kermel). Then, the homogeneous PVDF solution was heated in a water bath at 80 °C and stirred continuously for 5 h to completely dissolve the polymer until a clear and bubble-free solution was obtained. Subsequently, the electrospinning process (BJTechNOVA, TEADFS-100) was performed at a positive high voltage of 15 kV and a negative one of 1.5 kV, allowing a spacing of 15 cm between the needle tip and a grounded rotating drum collector (200 rpm). Next, the PVDF solution was transferred into a plastic syringe and injected at a flow rate of 1.5 ml h^{-1} using a syringe pump. Finally, the sample was removed from the collector to obtain the PVDF nanofiber membrane.

Fabrication of the SAWS: First, an array of cylindrical cavities was uniformly cut from the PET film using laser cutting technology to act as the cavity layer of the SAWS. Second, the removed PVDF nanofibers had to be cut to the same size and fixed on a transparent waterproof substrate, followed by the placement of the cut PET film on PVDF nanofibers and the even deployment of ZnS:Cu particles (Shanghai KPT Co.) with moderate weight in each cavity. Finally, the FEP film was covered with the cut PET layer, and the entire layer was pressed into an all-in-one device with waterproof edges using hot-pressing technology.

COMSOL Simulation: In the simulation, the dimensions of FEP film and PVDF nanofibers were 160 × 50 μm^2 and 160 × 20 μm^2, respectively, with a space of 150 μm. The diameter of the ZnS:Cu phosphors were set to be 40 μm. The charge densities on the FEP film, PVDF nanofibers, and ZnS:Cu phosphors were set to −3.5 μC m^{-2}, −55 μC m^{-2}, and +58.5 μC m^{-2}, respectively. The entire setup was surrounded by an earthed air square with a side length of 600 mm. The dielectric constants used in the simulation were $\varepsilon = 1.0$ for air, $\varepsilon = 2.4$ for FEP film, $\varepsilon = 9.3$ for PVDF nanofibers, and $\varepsilon = 8.6$ for ZnS:Cu phosphors.

Characterizations: Field emission SEM (SEM, Nova Nano 450, FEI, Japan) was used to take all SEM images. XRD (XRD system d8-advance, Bruker AXS GmbH, Germany) was utilized to characterize the cavity structure at room temperature. An ultraviolet-visible-near-infrared (UV-Vis-NIR) light source (UV-3600, Shimadzu, Japan) was adopted to analyze the transmittance of the FEP film and PVDF nanofibers. A spectrometer (Nova, Idea Optics, China) that has perpendicularly arranged optical fibers with a collimating lens was applied to observe optical emission. A transient- and steady-state fluorescence spectrometer (FLS-980, Edinburgh, England) was also employed to measure PL spectra.

Supporting Information

Supporting Information is available from the Wiley Online Library or from the author.

Acknowledgements

Z.T. and L.S. contributed equally to this work. This research was supported by HKSAR General Research Fund (14202121), the National

Natural Science Foundation for Young Scientists of China (No. 61804042) and the Research Project for High-level Talents in Hebei University (No. 521000981220).

Conflict of Interest

The authors declare no conflict of interest.

Data Availability Statement

The data that support the findings of this study are available from the corresponding author upon reasonable request.

Keywords

all-optical, self-powered, ultrafast response time, ultrahigh sensitivity, ultrasonic sensors, underwater, wireless

Received: September 29, 2021
Revised: November 10, 2021
Published online: December 23, 2021

[1] L. M. Jiang, Y. Yang, Y. Chen, Q. F. Zhou, *Nano Energy* **2020**, *77*, 105131.
[2] J. H. Bang, K. S. Suslick, *Adv. Mater.* **2010**, *22*, 1039.
[3] D. Seo, R. M. Neely, K. Shen, U. Singhal, E. Alon, J. M. Rabaey, J. M. Carmena, M. M. Maharbiz, *Neuron* **2016**, *91*, 529.
[4] Q. F. Shi, T. Wang, C. Lee, *Sci. Rep.* **2016**, *6*, 24946.
[5] L. M. Jiang, Y. Yang, R. M. Chen, G. X. Lu, R. Z. Li, J. Xing, K. K. Shung, M. S. Humayun, J. G. Zhu, Y. Chen, Q. F. Zhou, *Adv. Funct. Mater.* **2019**, *29*, 1902522.
[6] Q. F. Shi, T. Wang, T. Kobayashi, C. K. Lee, *Appl. Phys. Lett.* **2016**, *108*, 193902.
[7] Z. H. Shao, Q. Z. Rong, F. Y. Chen, X. G. Qiao, *Opt. Express* **2018**, *26*, 10820.
[8] X. H. Bai, M. L. Hua, T. T. Gang, Q. Tian, *Opt. Laser Technol.* **2019**, *112*, 467.
[9] X. X. Liu, D. Y. Chen, D. F. Yang, X. Y. Chen, X. H. Le, J. Xie, *IEEE Electron Device Lett* **2019**, *40*, 965.
[10] H. Mohapatra, M. Kleiman, A. Esser-Kahn, *Nat. Chem.* **2017**, *9*, 135.
[11] P. Zhu, Y. Chen, J. Shi, *Adv. Mater.* **2020**, *32*, 2001976.
[12] L. L. Zhao, Y. Zhang, F. L. Wang, S. C. Hu, X. N. Wang, B. J. Ma, H. Liu, Z. L. Wang, Y. H. Sang, *Nano Energy* **2017**, *39*, 461.
[13] Y. Chen, X. L. Bao, C.-M. Wong, J. Cheng, H. D. Wu, H. Z. Song, X. R. Ji, S. H. Wu, *Ceram. Int.* **2018**, *44*, 22725.
[14] D. Kuscer, F. Levassort, M. Lethiecq, A.-P. Abellard, M. Kosec, *J. Am. Ceram. Soc.* **2012**, *95*, 487.
[15] Z. Wang, Q. T. Xue, Y. Q. Chen, Y. Shu, H. Tian, Y. Yang, D. Xie, J. W. Luo, T. L. Ren, *Sensors* **2015**, *15*, 2538.
[16] X. L. Yin, Y. D. Shen, D. Su, Z. H. Shao, *Opt. Commun.* **2019**, *453*, 124422.
[17] H. Y. Li, J. M. Lv, D. L. Li, C. Y. Xiong, Y. H. Zhang, Y. T. Yu, *Opt. Express* **2020**, *28*, 18431.
[18] F. R. Fan, Z.-Q. Tian, Z. L. Wang, *Nano Energy* **2012**, *1*, 328.
[19] Z. L. Wang, *Adv. Energy Mater.* **2020**, *10*, 2000137.
[20] X. Liang, T. Jiang, Y. W. Feng, P. J. Lu, J. An, Z. L. Wang, *Adv. Energy Mater.* **2020**, *10*, 2002123.
[21] Y. Xi, J. Wang, Y. L. Zi, X. G. Li, C. B. Han, X. Cao, C. G. Hu, Z. L. Wang, *Nano Energy* **2017**, *38*, 101.
[22] R. Hinchet, H.-J. Yoon, H. Ryu, M.-K. Kim, E.-K. Choi, D.-S. Kim, S.-W. Kim, *Science* **2019**, *365*, 491.
[23] C. Chen, Z. Wen, J. H. Shi, X. H. Jian, P. Y. Li, J. T. W. Yeow, X. H. Sun, *Nat. Commun.* **2020**, *11*, 4143.
[24] H. Ouyang, Z. Li, *Sci. Bull.* **2019**, *64*, 1565.
[25] X. Zhao, Z. Zhang, Q. L. Liao, X. C. Xun, F. F. Gao, L. X. Xu, Z. Kang, Y. Zhang, *Sci. Adv.* **2020**, *6*, 4294.
[26] X. Y. Wei, X. D. Wang, S. Y. Kuang, L. Su, H. Y. Li, Y. Wang, C. F. Pan, Z. L. Wang, G. Zhu, *Adv. Mater.* **2016**, *28*, 6656.
[27] D. Peng, Y. Jiang, B. Huang, Y. Du, J. Zhao, X. Zhang, R. Ma, S. Golovynskyi, B. Chen, F. Wang, *Adv. Mater.* **2020**, *32*, 1907747.
[28] Y. J. Zhao, D. F. Peng, G. X. Bai, Y. Q. Huang, S. Q. Xu, J. H. Hao, *Adv. Funct. Mater.* **2021**, *31*, 2010265.
[29] L. Su, H. L. Wang, Z. Tian, H. J. Wang, Q. Cheng, W. Yu, *Adv. Sci.* **2019**, *6*, 1901980.
[30] X. J. Zhao, S. Y. Kuang, Z. L. Wang, G. Zhu, *Nano Energy* **2020**, *75*, 104823.
[31] H.-J. Park, S. M. Kim, J. H. Lee, H. T. Kim, W. Seung, Y. Son, T. Y. Kim, U. Khan, N.-M. Park, S.-W. Kim, *ACS Appl. Mater. Interfaces* **2019**, *11*, 5200.
[32] L. Su, Z. Y. Jiang, Z. Tian, H. L. Wang, H. J. Wang, Y. L. Zi, *Nano Energy* **2021**, *79*, 105431.
[33] X. Y. Wei, H. L. Wang, Y. Wang, S. Y. Kuang, X. X. Zhu, J. Z. Zou, L. Wang, X. R. Zeng, F. Rao, G. Zhu, *Nano Energy* **2019**, *61*, 158.
[34] C. H. Song, S. C. Zhu, L. R. Ma, Y. Tian, J. B. Luo, *Appl. Mater. Today* **2021**, *24*, 101081.
[35] X. Y. Wei, L. Liu, H. L. Wang, S. Y. Kuang, X. Zhu, Z. L. Wang, Y. Zhang, G. Zhu, *Adv. Mater. Interfaces* **2018**, *5*, 1701063.
[36] H. L. Wang, L. Su, H. Y. Li, Z. L. Wang, G. Zhu, *Mater. Horiz.* **2020**, *7*, 1144.
[37] Y. Wang, H. L. Wang, H. Y. Li, X. Y. Wei, Z. L. Wang, G. Zhu, *ACS Appl. Mater. Interfaces* **2019**, *11*, 13796.
[38] F. Q. Chen, Y. H. Wu, Z. Y. Ding, X. Xia, S. H. Li, H. W. Zheng, C. L. Diao, G. T. Yue, Y. L. Zi, *Nano Energy* **2019**, *56*, 241.
[39] M. C. Wong, L. Chen, G. X. Bai, L. B. Huang, J. H. Hao, *Adv. Mater.* **2017**, *29*, 1701945.
[40] S. H. Pan, Z. N. Zhang, *Friction* **2019**, *7*, 2.